Submersed Micropatterned Structures Control Active Nematic Flow, Topology and Concentration

Kristian Thijssen,[1,*] Dimitrius Khaladj,[2,*] S. Ali Aghvami,[3] Mohamed Amine Gharbi,[4] Seth Fraden,[5] Julia M. Yeomans,[1] Linda S. Hirst,[2,†] and Tyler N. Shendruk[6,‡]

[1] *The Rudolf Peierls Centre for Theoretical Physics, Department of Physics, University of Oxford, 1 Keble Road, Oxford OX1 3NP, UK*
[2] *Department of Physics, University of California, Merced, CA, 95343, USA*
[3] *Qlibrium, Woburn, Massachusetts 01801, USA*
[4] *Department of Physics, University of Massachusetts Boston, Boston, MA 02125, USA*
[5] *Physics Department, Brandeis University, Waltham, Massachusetts 02453, USA*
[6] *SUPA and School of Physics and Astronomy, The University of Edinburgh, Peter Guthrie Tait Road, Edinburgh EH9 3FD, United Kingdom*

Coupling between flows and material properties generally gives rheological matter its wide-ranging applicability, and this is particularly pronounced in active fluids for which internal structure and continuous energy injection lead to spontaneous flows and complex, out-of-equilibrium dynamics. We propose and demonstrate a convenient, highly tune-able method for controlling flow, topology and composition within active films. Our approach establishes rheological coupling via the indirect presence of fully submersed micropatterned structures within a thin, underlying oil layer. Simulations reveal that micropatterned structures produce effective virtual boundaries within the superjacent active nematic film due to differences in viscous dissipation as a function of depth. This accessible method of applying position-dependent, effective dissipation to the active films presents a non-intrusive pathway for engineering active microfluidic systems.

Active fluids are inherently out-of-equilibrium; they locally transform internal energy into material stresses that can result in spontaneous, hydrodynamic motion. An increasing number of bio-physical systems, including colonies of bacilliform microbes[1–4], cellular monolayers[5–9], and subcellular filaments[10–12] display such collective active motion, orientational order and topological singularities. Controlling active dynamics is essential not only to fully understanding how such biological systems employ self-generated stresses but also in order to develop active-microfluidic devices.

To this end, recent work considers how confining walls[13, 14], arrangements of obstacles[15, 16] and the dynamics of topological defects[17] dictate active nematic flow. Control of active material concentration has been studied from the perspectives of co-existence of phases in self-propelled rods[18–20] and motility-induced phase separation[21–23]. Controlled accumulation and depletion of active matter has been engineered in bacterial systems to concentrate cells[24, 25] and to drive bacterial-ratchet motors[26–28]. Similarly, substrate gradients modify cellular motility driving density variation[29] and directed migration[30, 31].

In addition to varying concentration and flow, topology has been controlled by including externally driven flows[32–34] and curvature[35, 36]. Recent work shows that locally altering activity modifies defect population[37], and anisotropic smectic sublayers below active nematic sheets can constrain orientation[38]. Such studies demonstrate how underlying sublayer properties have pronounced effects on active dynamics and suggest approaches for engineering control of active matter.

We propose a new micropattern-based method for controlling active nematic dynamics without contiguous contact with active films. By patterning oil-submersed solid substrates below 2D active nematic films with geometrical structures of differing height, we achieve effective virtual boundaries within active films that control topological defect populations, collective flow and concentration of active nematic material without penetrating the film. By implementing underlying submersed patterned microstructures, we tune the depth of the oil layer to adjust dissipation within the superjacent film and thereby generate a highly tune-able technique for controlling the active dynamics. Presently, we introduce four initial submersed structures: micropatterned trenches (**Figure 1**a-c), undulated substrates (**Figure S1**), stairways (**Figure 1**d-f), and pillars (**Figure 1**g-i).

To investigate how structures fully submersed in a layer of oil influence defect dynamics in the superjacent active film, we consider the trench geometry depicted in **Figure 1**a. An active nematic microtubule network is generated at an oil-water interface above a micropatterned trench of depth $\Delta_t = 18 \pm 1\mu$m and width $w_t = 327 \pm 2\mu$m fabricated using photolithography (**Methods I.2**). We observe that flows in the active nematic layer exhibit coexistence of two distinct regions: one directly above the trench and another in the shallows surrounding the trench (**Figure 1**b). These regions are separated by well-defined virtual boundary lines located directly above the trench edges. Beyond the trench boundaries, the active nematic retains the chaotic nature of active turbulence; however, within the boundaries, the trench width establishes a local confining length scale within the superjacent active nematic film (**Movie M1**). These virtual

* These authors contributed equally
† lhirst@ucmerced.edu
‡ t.shendruk@ed.ac.uk

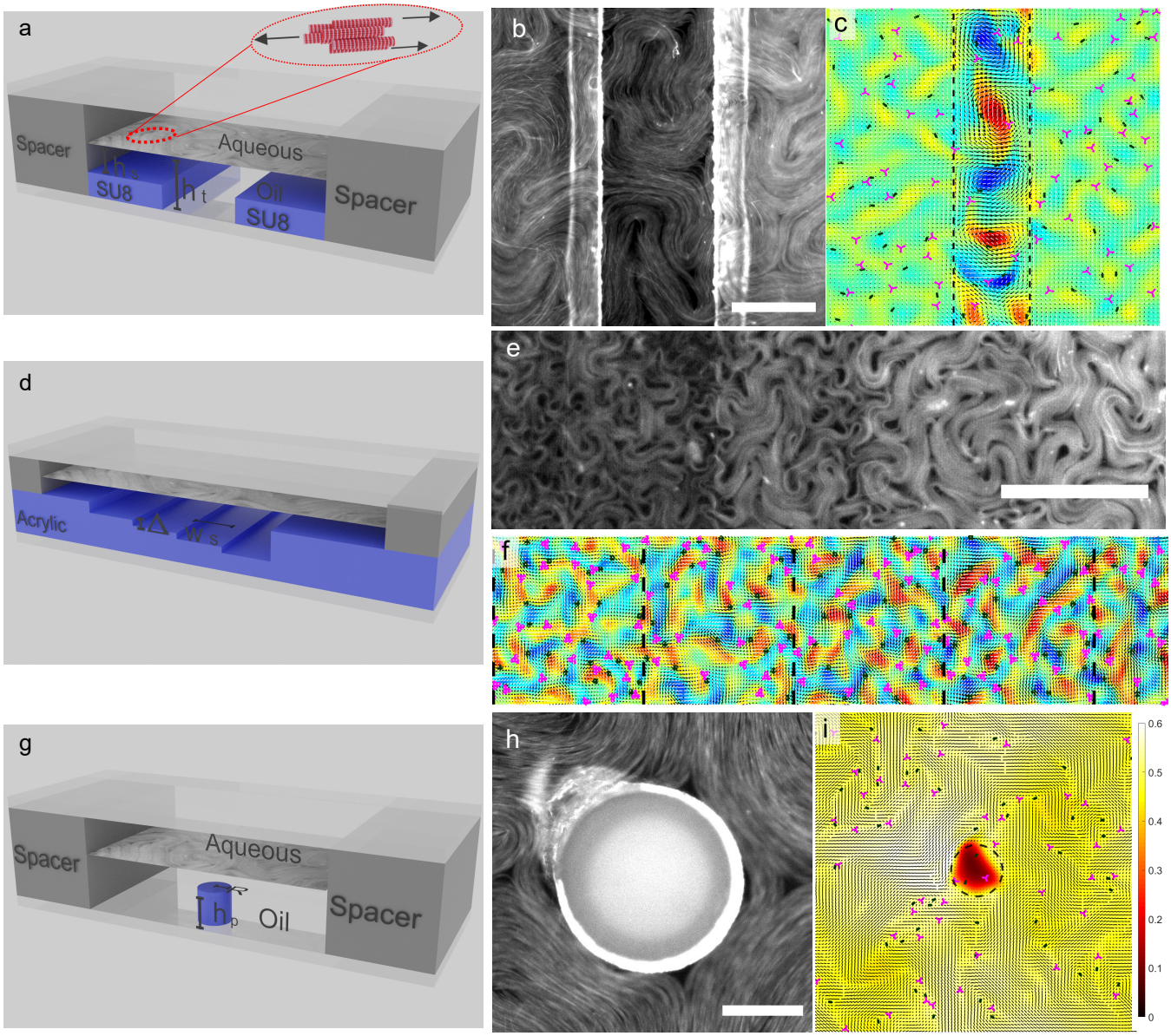

FIG. 1: **Submersed micropatterns control active nematic dynamics.** (a-c) **Trench set-up.** An active film resides at the oil-water interface above different substrate depths. The active flows drag the underlying oil layer but viscous dissipation is depth dependent, affecting active nematic film dynamics. (b) Fluorescent image of the submersed trench beneath the active nematic. Scale bar = 250μm. (c) Simulation results for vorticity field within the superjacent active nematic layer. Distinct flow behaviours are found within the low friction region (between the dashed lines) and high friction (beyond the dashed lines). Plus-half (minus-half) defects denoted by dark green (magenta) symbols behave differently in the two regions regions. (d-f) **Stairway set-up.** (e) Fluorescent image of micromilled stairway and the superjacent bundled-microtubule active nematic. Scale bar = 250μm. Step location indicated by dashed lines. (f) Simulations results for discrete steps in the effective friction (dashed lines). The differences in oil dept alter the length scale of the active turbulence above each step. (g-i) **Pillar set-up.** (h) Fluorescent image of the bundled-microtubule film above the SU-8 micropillar. Scale bar = 100μm. (i) Simulation results show the active nematic concentration ϕ is depleted within the high friction region encircled by the pillar perimeter (dashed line). Active material is not observed above the pillar.

walls trap defects in the trench region and produce active flow behaviours comparable to those observed in confining channels[39–42]. This result illustrates how effective virtual boundaries such as these, can be used to define areas of orderly flows and areas of active turbulence without penetrating the active film.

The $\pm 1/2$ topological defect distributions across the trench (**Methods I.4**) demonstrate that -1/2 defects tend to be located in the vicinity of the virtual boundary (**Figure 2**a). Experimental observations of -1/2 defect trajectories near the boundary reveal that they tend to linger over long intervals, contributing to high-frequency peaks (**Movie M1**). On the other hand, +1/2 defects tend to be depleted from the vicinity of the trench bound-

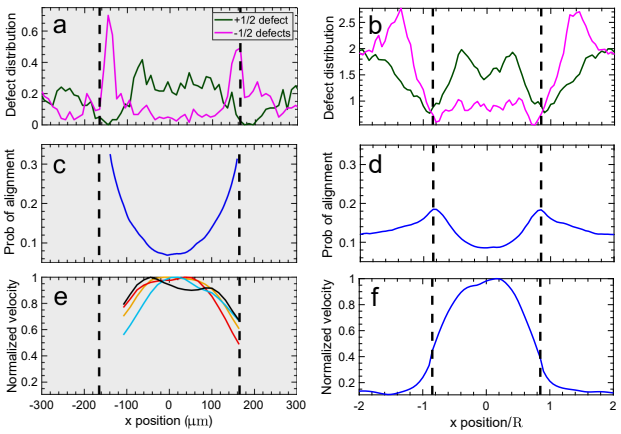

FIG. 2: **Positive defects depleted at the trench interface** (a-b) Distribution of +1/2 (dark green) and -1/2 (magenta) defects as a function of transverse position x measured from experiments and simulations respectively. Panels with shaded grey backgrounds denote experimental results, while non-shaded backgrounds denote numerical results throughout. (c-d) The probability profile that the nematic director is oriented less than 10° from the direction parallel to the trench wall as a function of x. The director field has a high probability of alignment with the virtual boundary. (e-f) Normalised root mean square fluid velocity profile across the trench.

ary and are confined within the trench region, moving along oscillatory trajectories that do not typically approach the boundaries (**Movie M1**). In the exterior region, far from the virtual trench, the defect density profile approaches a homogeneous distribution of positive and negative defects.

The effective virtual boundaries arise from abrupt steps in fluid depth $h(\boldsymbol{r})$ between the film and the underlying substrate at each point $\boldsymbol{r}$. The fluid depth h increases from h_s in the surrounding shallows to a trench depth $h_t = h_s + \Delta_t$ (**Figure 1**a). As activity drives flows within the nematic film, the underlying oil layer viscously dissipates momentum due to the subjacent no-slip substrate, which can be described as a local effective friction $\gamma(\boldsymbol{r})$ acting on each point within the superjacent active film[43]. Following from the lubrication limit, the effective friction coefficient scales as $\gamma \sim \eta'/h(\boldsymbol{r})$, where η' is an effective viscosity of the film and surrounding fluids. The abrupt height change across the trench boundaries results in sharp, virtual boundaries.

We replicate the observed experimental phenomena with 2D active nemato-hydrodynamic simulations, in which the submersed micropatterns are incorporated via an effective friction field (**Methods I.5**). Numerical results demonstrate that a step in effective friction can reproduce the experimentally observed active flows (**Figure 1**b) and introduce virtual boundaries in the active layer, which repel +1/2 defects (**Figure 2**a-b). This agreement between experimental and numerical defect distributions demonstrates how effective friction is the mechanism by which micropatterned structures create virtual planar boundaries and introduce a confinement length scale to the active nematic without penetrating the film. The -1/2 defect density peak at the virtual boundary (**Figure 2**a) is consistent with work[42] showing walls can act as catalysts for pair creation and unbinding: while newly created +1/2 defects move away due to self-propulsion, the -1/2 defects remain near the boundary.

While the experimental -1/2 defect density is peaked sharply in the vicinity of the virtual boundaries (**Figure 2**a), in simulations, it is broadened and peaked outside the trench region (**Figure 2**b). To understand this difference, we consider the time-averaged director orientation across the trench (**Methods I.4**; **Figure 2**c), which reveals that the virtual boundaries introduce effective planar anchoring of the director, similar to that seen for impermeable boundaries[42]. The model captures this behaviour, showing that the probability declines to a uniform distribution far from the trench (**Figure 2**d). Experiments exhibit stronger planar anchoring at the virtual boundaries than simulations, which is likely related to the model's assumption of a continuous fluid (**Methods I.5**) compared to finite-sized microtubule bundles. The stronger anchoring in the experiments constrains the -1/2 defects to the region inside the trench, while in simulations they are pushed to the outside of the boundaries (**Figure 2**a-b). In both experiments and simulations, +1/2 defects are trapped between the virtual boundaries.

The submersed trench not only impacts the nematic field but also generates a virtual boundary for the velocity field (**Figure 2**e-f). Superjacent to the trench, velocities are lower in the proximity of the trench boundary and maximum at the trench centre. Since activity varies slightly between experimental realisations, we normalise the flow profiles and compare to the decrease predicted by the model (**Figure 2**f). The virtual boundaries do not impose no-slip conditions but decrease the speed to the slower value of the surrounding active turbulence. The decreasing flow profile explains the preferential alignment of the microtubule bundles in the vicinity of the virtual boundaries (**Figure 2**c-d). Any orthogonal bundle midway over the boundary is subject to a large, axial, laminar flow inside and slow disorderly flows outside, which compete to produce an aligning torque.

The faster, orderly flow superjacent to the trench and slower, active turbulence in the exterior region call attention to the fact that active turbulence is a low-Reynolds number phenomenon[44]. Confinement and low friction above the trench generate rapid-but-orderly flows. On the other hand, the higher friction produces a smaller characteristic length scale[45], but also slower speeds in the shallows. Thus, the submersed micropatterned trench segregates rapid laminar flow above the trench and slow-but-disorderly active turbulence outside.

Because the submersed micropatterned trench produces virtual boundaries that introduce a confining length scale, the competition between confinement and intrinsic active nematic length scale can be probed.

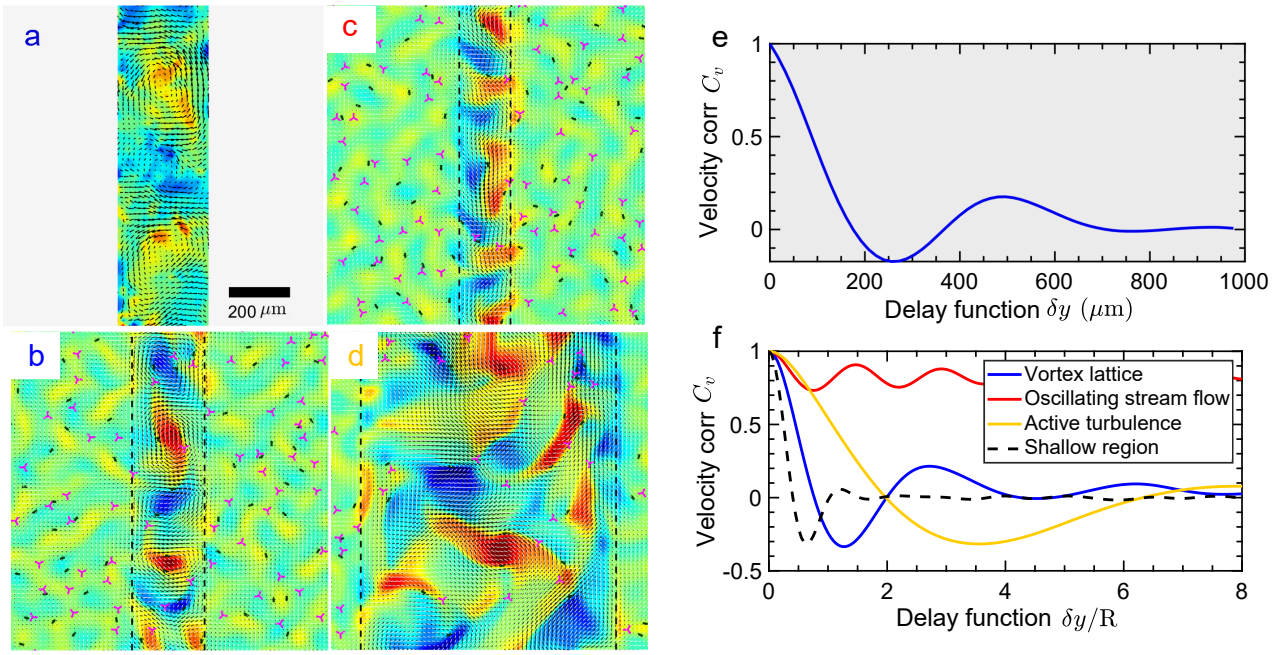

FIG. 3: **Friction boundaries result in separate flow regions.** (a) Instantaneous experimental vorticity superjacent the deep trench region from PIV for a trench of width $w_t = 325\mu$m. Panels with shaded grey backgrounds denote experimental results, while non-shaded backgrounds denote numerical results. (b) Simulation snapshot of a repeating lattice of counter-rotating vortices above a trench of width $w_t = 1.7R$ (**Methods I.5**). Plus-half defects (dark green) are trapped between the virtual boundaries, generating the repeating vortex structure along the centre line that is distinct from the active turbulence that exists outside the virtual boundaries. (c) Decreasing the trench width to $w_t = 1.2R$ results in long-range, oscillatory, bidirectional streaming flow inside the trench. (d) Increasing the trench width to $w_t = 6R$ results in active turbulence both inside and outside the trench region, but with differing intrinsic length scales due to the different effective frictions. (e) The velocity-velocity autocorrelation function $C_v(\delta y) = \langle \boldsymbol{v}(\boldsymbol{r};t) \cdot \boldsymbol{v}(\boldsymbol{r} + \delta y\, \hat{\boldsymbol{y}}; t) \rangle \,/\, \langle v^2 \rangle$ for the experiment illustrated in (a), measured a distance δy along the the $x = 0$ centre line of the trench. Due to the confinement effect, long-range flow structures are formed in the low-friction regime epitomised by the strong correlation-anti-correlation-correlation signal. (f) The autocorrelation function from the simulations shown in b (blue), c (red), d (green) and the shallow region outside the virtual channel (dashed). The blue curve displays pronounced correlation and anti-correlation indicating the counter-rotating vortex pattern (b), which corresponds to the behaviour observed in the presented experiments (a,e). The red curve is long-lived and fully correlated in the narrow channels (c), while the green curve decorrelates to zero after an anti-correlation, signalling active turbulent behaviour within the virtual boundaries as well as outside.

Movie M1 and **Figure 3**a experimentally demonstrate that a recurrent vorticity structure is established between the virtual boundaries when active and confining scales coincide[16, 39] (**Figure 3**b and **Movie M2**). Examining the velocity autocorrelation functions quantifies the different flow profiles above the trench (**Figure 3**e and f; blue curve). The correlation function exhibits repetition between correlated and anti-correlated regions due to repeating clock-wise and anti-clockwise vortices. Active turbulence exists outside of the virtual channel, as characterised by an immediate initial drop in the correlation (**Figure 3**f; dashed curve).

In narrower or wider confinements, the flow transitions to other states (**Figure 3**c-f). In the narrow trench (**Figure 3**c), the flows are long-ranged, bidirectional and oscillatory with a preference for aligning with the boundaries (**Figure 3**f). This oscillatory-streaming state occurs when the confining length scale w_t is small compared to the low-friction intrinsic active nematic length scale[39]. The increased trench width allows active turbulence in both the area superjacent to the trench and the shallow exterior regions (**Figure 3**d) but with differing active nematic length scales (**Figure 3**f).

The trench geometry demonstrates that submersed microstructure patterning can impose confining virtual boundaries and is a feasible technique for maintaining coexistence of distinct flow behaviours simultaneously at different locations in a single active nematic layer. A strength of our submersed-micropatterned-structure approach is that the boundaries act without physically penetrating the film and so active material does not first have to saturate a cavity before confinement dynamics can be explored[46]. Filling complex geometries with filament-based active material may be the prohibitive step in active microfluidics[47]. The proposed micropatterned method circumvents these difficulties, opening possibilities for experiments involving more complex geometries and fine-tuned positional control.

While the trench geometry demonstrates that micropatterns with precipitous edges can actualise abrupt

boundaries within superjacent active films, the ability to gradually tune the effective friction through gradients in oil-layer thickness allows our technique to gently guide defect dynamics. To demonstrate this, an undulating effective friction is produced by fully submersing a micropattern sinusoidal substrate (**Methods I.3**) characterised by amplitude $\Delta_u = 40 \pm 2\mu$m and wavelength $\lambda_u = 150 \pm 2\mu$m. Unlike the trench geometry, the sinusoid system does not separate into distinct coexisting flow states (**Movie M3**). Rather, the resulting anisotropic friction gradients present a means of orientation-control of motile defects. Self-propelled +1/2 defects orient and travel in trains above the troughs (**Figure S1**a). Motile defects move through the system subject to friction gradients when they have components perpendicular to the troughs, such that trajectories co-aligned with the troughs minimise dissipation, causing the observed parallel/anti-parallel laning of +1/2 defects.

However, such trains of +1/2 defects do not persist indefinitely since the trains produce nematically ordered regions, which are susceptible to the extensile-active nematic hydrodynamic-bend instability[48–50] causing pair creation events that inevitably destabilise the flow (**Movie M3**). Since initially unbound +1/2 defects are typically oriented perpendicular to the nematic ordered lanes (**Figure S1**b), producing a crosshatched trajectory pattern. These dynamics are not nearly as pronounce in sinusoid systems with a larger wavelengths ($\lambda_u = 500\mu$m; **Movie M4**). Positive defects that are oriented up the friction gradient exhibit the same deflected motion as in the smaller system and so the motile defects show some alignment along the troughs but the crosshatched dynamics are indiscernible. The sinusoid geometry demonstrates that submersed micropatterned structures can fine-tune the active flow and nematic structure, thereby offering a means to guide and control defect dynamics.

We now present a substrate patterned as submersed stairway (**Figure 1**d) designed to simultaneously observe active turbulence, with a gradient in characteristic length and time scales with the same ATP concentration (**Movie M5**). Individual steps are micro-milled to possess horizontal width $w_s = 500 \pm 2\mu$m and height of $\Delta_s = 10 \pm 1\mu$m (**Methods I.3**). The fluid depth is $h(\boldsymbol{r}) = h_0 + \Delta_s n(x)$, for step number n and initial fluid depth $h_0 = 12 \pm 3\mu$m, determined through confocal microsopy (**Methods I.3**). We focus on $5 \leq n \leq 9$ for which the microtubule network forms a well-defined, continuous nematic field (**Figure 1**e; **Movie M5**). As the depth increases with n, the effective dissipation within the oil-layer decreases, which we simulate via discrete steps in effective friction in the superjacent active film (**Figure 1**f; **Methods I.5**).

Above the step pattern, the active length scales increase with decreasing friction, as characterised by the defect distribution (**Figure 1**e-f; **Figure 4**a; **Movie M5**). Within each step the distribution is flat. However, at each edge, the number density of -1/2 defects peaks, while the density of +1/2 defects plunges. This is consistent with defect densities at the edges of the

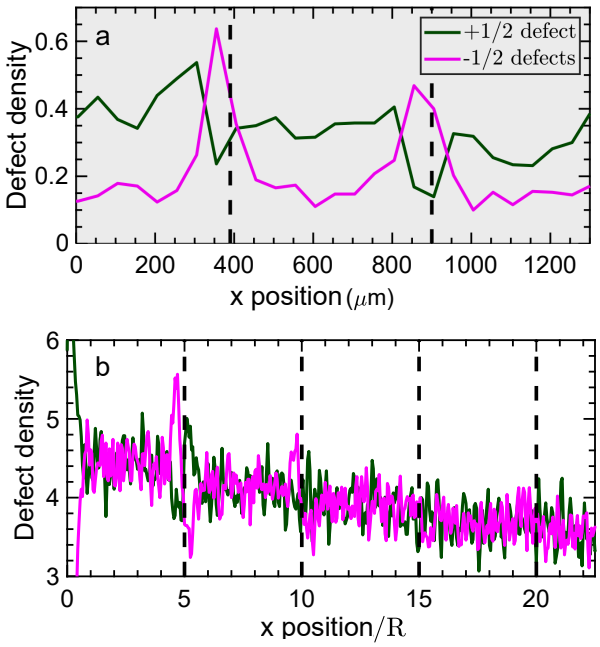

FIG. 4: **Submersed micropatterned stairway allows simultaneous coexistence of regions of separated active turbulence with differing defect densities, with the same ATP concentration.** Plus (dark green) and minus (magenta) defect distribution as a function of position down the stairway x. (a) Measurements from experiments for steps of width $w_t = 500\mu$m (grey shaded background). (b) Measurements from simulations for steps of width of width $w_t = 5R$ (non-shaded background).

trench (**Figure 2**a-b). Though the edge peaks are less pronounced than in experiments, numerical results more clearly show the decrease in defect density across multiple steps. The change in defect density is modest, consistent with studies demonstrating that increasing oil viscosity five orders of magnitude only increases defect density by a factor of order unity[51], which highlights the potential tunability of our method. Interestingly, we only observe a continuously well-defined nematic field for oil-depths that are much greater than h_0 in both experiments and simulations (**Figure 1**d). For small n, the active film exhibits disorderly textures akin to those observed in experiments utilising high viscosity oils[51]. The film develops gaps causing the definition of singularities in the nematic field to become tenuous, and the film is no longer necessarily in an unambiguously ordered phase. This suggests that submersed micropatterned structures can do more than impact flow and orientational state: we now demonstrate how substrate micropatterning can be used to control active matter concentration via structures raised above the solid substrate yet still fully submersed in the underlying oil-layer.

We consider submersed SU-8 pillar structures (**Figure 1**g) of radius $r_p = 116 \pm 2\mu$m and height $h_p = 6.8 \pm 0.3\mu$m. As in the trench, sinusoid and stairway geometries, the active nematic layer is subject

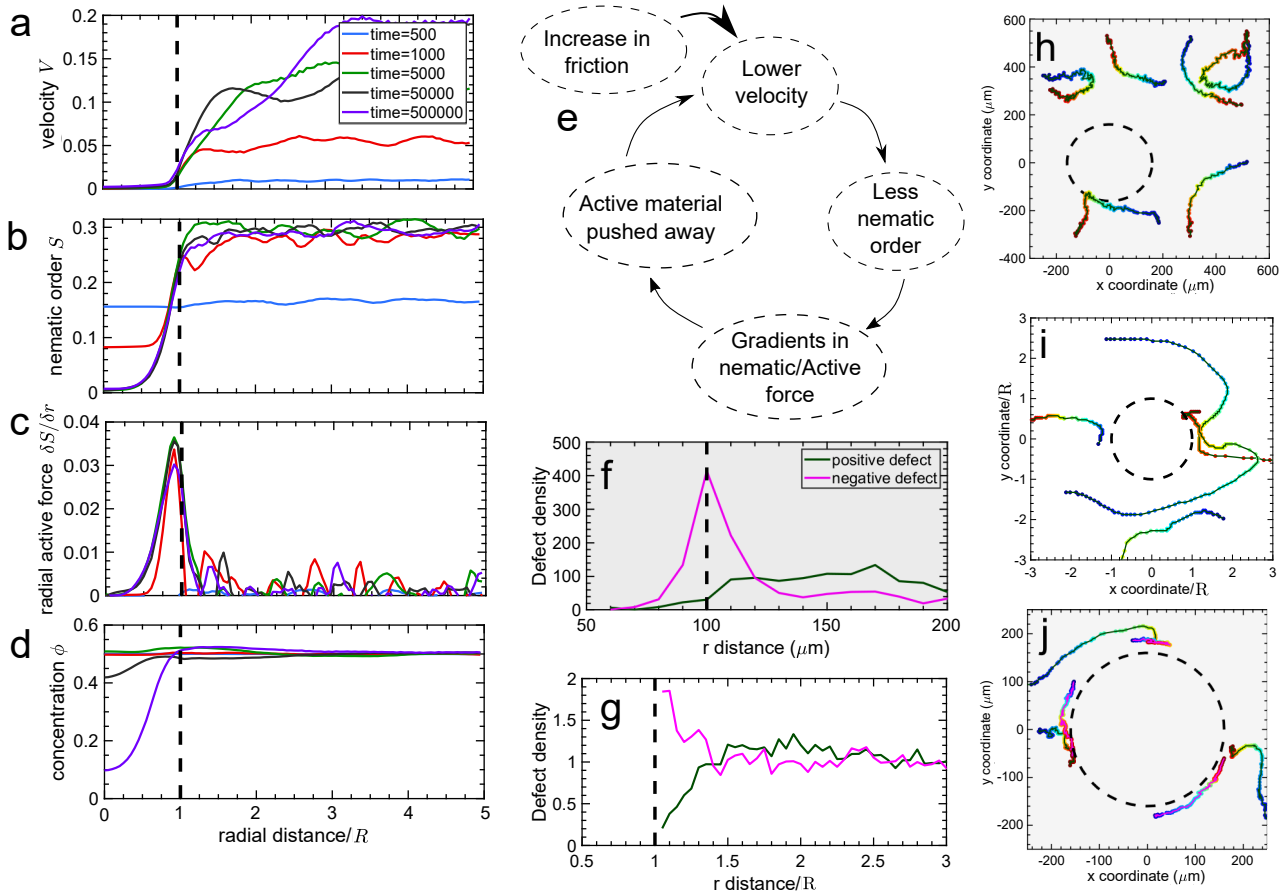

FIG. 5: **Pillars cause local high friction regions which result in active matter depletion.** (a) Due to the higher friction, the flow in the active nematic film is remains low. (b) The nematic is highly ordered far from the pillar but disordered above it because the speed is lower in the higher friction region. (c) The difference in nematic order at the friction interface results in a radial active force. (d) This radial active force pushes the active material concentration outwards resulting in depletion effects. Panels with non-shaded backgrounds denote numerical results, while shaded grey backgrounds denote experimental measurements. (e) Schematic of a-d. (f-g) +1/2 (dark green) and -1/2 (magenta) defect distribution as a function of radial distance from a submersed pillar from experiments (f) and simulations (g). (h-j) xy trajectories of example $\pm 1/2$ defects dynamics in the vicinity of the pillar. Dark green (magenta) lines denote +1/2 (-1/2) defects. Time along the trajectory is displayed as circular markers coloured blue at the initial time and changing to red at the final instant. (h-i) +1/2 defects deflecting from the pillar; experiments (h) and simulations (i). (j) Experimental xy trajectories of +1/2 defects absorbing to the pillar boundary through defect annihilation with -1/2 residing in the vicinity of the perimeter.

to a step-change in the effective film friction. However, differentiating it from previous structures, the pillar's virtual boundary forms a closed loop. The most prominent effect is a pronounced dilution of active material from the enclosed region above the pillar (**Figure 1**h; **Movie M6**), which is recapitulated in the simulations (**Figure 1**i; **Movie M7**). The phase-field active material concentration $\phi(\boldsymbol{r};t)$ (**Methods I.5**) demixes in the high effective friction region directly above the pillar.

To understand the mechanism leading to the pillar-bound dilute phase of active matter, we consider a simplified model of the active nematic. The effective friction is locally large above the pillar, causing the flow speed to decrease in the enclosed area but remain non-zero beyond the pillar border (**Figure 5**a). Since nematic ordering arises in active microtubule network films due to activity-induced motion, the sharp decrease in flow causes a corresponding drop in scalar order S across the circular virtual border (**Figure 5**b). However, the abrupt gradient in S produces a radially outward average active force $\boldsymbol{f}(r;t) \sim \langle \boldsymbol{\nabla} \cdot \mathbf{Q}(\boldsymbol{r};t) \rangle \approx \partial_r \zeta(r;t) S(r;t) \hat{\boldsymbol{r}}$ (**Equation 6** of **Methods I.5**), when the variation of the nematic order is dominated by the radial change in scalar order parameter and bend-induced stresses are neglected. Thus, the active forcing is expected to be radially outward and sharply peaked about the interface as observed in simulations (**Figure 5**c).

However, activity does not simply produce increased pressure across the perimeter but rather is able to selectively deplete the concentration of active material ϕ. Since the active film is considered incompressible, fluid mass density is constant and hence divergence of the film velocity is zero (**Equation 3** of **Methods I.5**). Thus,

depletion demands that outward advection is more frequent in regions where ϕ is larger on average. This is indeed the case because the activity depends on the local amount of active material present, $\zeta(r;t) = \zeta_0\phi(r;t)$ (**Equation 7** of **Methods I.5**), which causes the radially outward forcing to be stronger in magnitude where ϕ is large. For this reason, if the surrounding active turbulence stochastically advects ϕ-rich active material across the perimeter, the local active forces increase in kind to selectively repulse the material from the dissipative region (**Figure 5**d; **Movie M7**) but if ϕ-poor fluid enters the local active force decrease allowing the fluid to more easily cross the perimeter. Thus, the depletion of active matter above the pillar is a result of the high effective friction lowering the velocity causing nematic discomposure and selectivity due to the direct dependence of activity on the local concentration (**Figure 5**e).

Noting that the highest steps in the stairway geometry also fail to exhibit continuous nematic fields but are not devoid of active matter (**Figure 1**d; **Movie M5**), we test if the curvature of the virtual barriers impacts depletion by simulating a rectangular pillar (**Figure S2**). We observe a comparable depletion of ϕ from the enclosed area as in the circular pillar and so conclude that curvature is not the critical difference. Secondly, we consider a circular pit and find that active material accumulates in the enclosed area, consistent with the explanation of the depletion mechanism (**Figure S3**). We conclude that accumulation or depletion of active material using submersed micropatterned structures relies principally on two attributes: (i) The oil-layer must be thin (high effective friction) to suppress the active flows necessary to exhibit nematic order. (ii) An enclosed area must be circumscribed by a virtual boundary to prohibit longitudinal active streams through the incompressibility constraint.

In addition to controlling concentration, submersed pillars interact with defects. We observe a greater frequency of -1/2 defects in the vicinity of the virtual boundary in our simulations (**Figure 5**f-g). The planar anchoring of the director field explains the distribution of defects at the pillar boundary (**Figure 1**h-i). The resulting bend deformation around the perimeter drives hydrodynamic instabilities to continually generate defect pairs, with newly created self-motile +1/2 defects typically oriented radially away from the centre such that they swiftly move away from the interface (**Movie M8**), leaving unbound immotile -1/2 defects behind (**Figure 2**f-g). Submersed pillars can also serve as a virtual obstacle for defect trajectories (**Movie M8**). Positive defects that approach the pillars from the surrounding turbulence stall or are deflected once in proximity to the pillar (**Figure 5**h-j). Deflected +1/2 defects first slow as they approach the pillar, then scatter and regain speed as they move away from the submersed structure (**Figure 5**h-i). Positive defects that stall as they approach the boundary temporarily hold their position before annihilating with pillar-associated -1/2 defects (**Figure 5**j). While defects can temporarily enter the depleted area, such infrequent events are transient (**Movie M9**) as the repulsive active force (**Figure 5**c) pushes such incursions radially outward.

Using a combined experimental and simulation approach, we have demonstrated that micropatterns fully submersed in an underlying oil layer can guide the flow, topology, and even concentration of active material in superjacent nematic films without direct contact. By imposing changes in substrate depth, viscous dissipation in the oil layer enacts a position-dependent effective friction coefficient on the active material. Abrupt substrate height steps can constitute sharp virtual boundaries in the active matter layer, which can control flow and defect behaviour. As proof-of-concept systems, we presented virtual channels exhibiting coexisting flow states, sinusoid substrates that gently guide defects, stairways separating active turbulence with differing characteristic length and time scales, and a virtual enclosure depleted of active material that acts as an obstacle scattering nearby defects.

The proposed technique of fully submersing micropatterned structures facilitates new approaches for fabricating complex active topological microfluidic devices. For example, complications associated with infiltration of active nematics into confined spaces could be avoided, and active dynamics in various geometries at the same activity could be compared directly. Furthermore, locally concentrating or depleting active material could regulate activity at constant levels of ATP or rheological properties such as film viscosity or nematic elastic coefficient through this novel approach.

I. METHODS

I.1. Formation of the Active Nematic Network

An active nematic microtubule network is generated following the protocol previously reported by Sanchez *et al.* at an oil-water interface[52]. Prior to experiments, active premixtures are prepared in 3.73µm aliquots containing biotin-labeled K401 kinesin motors, streptavadin, PKLDH, phosphoenol pyruvate (PEP) (used for ATP regeneration), 4mg/ml glucose, 0.27mg/ml glucose oxidase, 47µg/ml catalase and 2mM Trolox, and 6% (w/v) 20kD polyethylene glycol (PEG) in M2b buffer (80mM PIPES pH6.8, 2mM $MgCl_2$, and 1mM EGTA). To prevent photobleaching during imaging, premixtures contain 6.65nM DTT, an antioxidant solution. Once the premix is prepared, the aliquots are flash frozen in liquid nitrogen and promptly stored at $-80°$C for future use.

To perform active nematic experiments, 1mM ATP (final concentration) is added to the 3.73µm premixture aliquot followed by 2µl of 6mg/ml (3%) Alexa Fluor 647 labeled GMPCPP microtubules (for a final concentration of 1mg/ml). For fluorescence imaging, microtubules are fluorescently labelled with Alexa Fluor 647[52]. The result is a suspended active nematic with a total volume of 6µl. We use an ATP concentration at saturation (*i.e.* the local microtubule extension speed was maximised).

To confine the active nematic at an oil/water interface, we follow the previously published procedure[17, 52]. We first create a flow cell made from the glass substrate with patterned structures, double-sided tape and a coverslip treated with a polyacrylamide brush (**Figure 1**). The polyacrylamide brush prevents excess protein binding to the coverslip.

We flow in an oil/surfactant mixture (3M HFE7500 with 1.8% PFPE-PEG-PFPE (perfluoropolyether) surfactant) into the channel. Then, this mixture is exchanged with the active microtubule network. This system forms a 3D, unconfined, active microtubule network. Streptavidin can bind up to four biotin-labeled kinesin molecules and when microtubules of opposing polarities align parallel to each other, the kinesin molecules oriented at 180° to each other walk in opposite directions along those neighbouring microtubules. As the kinesins walk, the filaments produce an extensile motion driven by ATP hydrolysis. The ends of the flow cell are sealed using a UV-curable glue (RapidFix). The active layer is then centrifuged using a swinging bucket rotor for 42 min at 300rpm.

I.2. Photolithography

The trench and pillar geometries are produced using photolithography. SU-8 (MicroChem Corp.) is a negative tone epoxy-based photoresist that is used to create thin film plastics on substrates. SU-8 is composed of epoxy-based monomers and photo-acid generators (PAGs) suspended in a solvent. Upon exposure to ultra-violet (UV) light, the PAGs release acids serving as a catalyst for cross-linking available epoxy groups on the monomer once heat is applied to the substrate. Prior to fabrication, glass substrates are thoroughly cleaned in soap and water followed by 30 minutes of sonication in acetone, methanol and ethanol in this order. The glass substrates are rinsed in nanopure water to ensure minimal presence of surface contaminants. The glass is then plasma treated with oxygen for 2 minutes. To ensure the removal of residual moisture left on the surface, the glass substrate is placed on a hotplate for 5 minutes at 200°C; the substrate is left to cool down to room temperature for 5 minutes in a humidity-controlled area.

Upon thorough cleaning, a quarter-sized drop of SU-8 50 is deposited on the glass substrate. The SU-8 is spin-coated at 2000rpm for 45 seconds followed by a 10 minute wait. The substrate is then soft baked at 65°C for 12 minutes then at 95°C for 45 minutes on a hotplate to evaporate solvent. The substrate is again left to cool to room temperature with another wait of 10 minutes. The film is then exposed to 365nm UV light (500mJ/cm^{-2}) followed by a 10-minute wait step. To crosslink the exposed regions' epoxy groups, the substrate undergoes a post exposure bake for 5 minutes at 65°C then for 15 minutes at 95°C on a hot plate. After the 15 minute bake, the hot plate is turned off and allowed to cool to room temperature without the removal of the coated substrate. This step is to avoid thermally shocking the film which can result in cracks and poor adhesion. The substrate is developed for 30 minutes with gentle agitations. Once developed, the residual SU-8 developer is rinsed with isopropanol and de-ionised water then dried with nitrogen gas. After development, the substrate is then hard baked for 2 minutes at 150°C. The heights of the microstructures are measured using profilometry.

I.3. Micro-milling

The stepped substrate and the sinusoid surface are produced using the computer numerical controlled (CNC) micro-milling We use the milling machine TN5-V8-TC8 (MDA Precision) to fabricate the microstructures on a poly(methyl methacrylate), known as acrylic. This machine is capable of handling drills and endmills as small as 50μm in diameter and has a spindle rotational accuracy of around 2μm. The first designed system has steps (height), each with a rise of $\Delta_s = 10\mu\text{m} \pm 1$ and a run (horizontal width) of $w_s = 500\mu\text{m} \pm 2$. The system is composed of ten steps. The smaller of the two sinusoid systems has undulations with a peak-to-peak amplitude $\Delta_u = 40 \pm 2\mu\text{m}$ and a wavelength $\lambda_u = 150 \pm 2\mu\text{m}$, while the larger has a peak-to-peak amplitude $\Delta_u = 50 \pm 2\mu\text{m}$ and a wavelength $\lambda_u = 150 \pm 2\mu\text{m}$. These features are first transferred into a soft elastomer, polydimethylsiloxane (PDMS), and then into a cyclic olefin copolymer (COC), using a thermopress. The COC sheets of thickness ranging from 150μm to 350μm are then immersed for one hour in a solution of 10wt% of 8-Anilino-1-naphthalenesulfonic acid (ANS), dissolved in a mixture of 85wt% ethanol and 15wt% decalin. This treatment helps add a fluorescent layer of ANS dye to the COC surface, which allows measuring the fluorinated oil's thickness under the active nematic, using a Leica SP8 UV/Visible Laser Confocal Microscope. The confined active nematic is imaged using a wide-field fluorescent Nikon Eclipse Ti-E microscope with an Andor Clara camera controlled by *Micromanager* open-source software.

I.4. Data processing

To investigate how defect dynamics in the active layer are influenced by submersed structures, labeled microtubule bundles are imaged using fluorescence microscopy. Four-hundred-frame videos are collected at 1 frame per second and processed using Fiji/ImageJ version 1.52a software. To acquire defect distributions, active nematic microtubule defects are identified and counted manually every 10 frames for each video. Two-dimensional Cartesian components for both x and y axes are acquired from both +1/2 and -1/2 defects using the *Click for position plugin* on Fiji/ImageJ. For the submersed trench geometry, we use MATLAB to analyse the frequency and position for both +1/2 and -1/2 defects across the channel. Defects are organised and binned in 10μm horizontal in-

crements across the field of view.

For the stairway geometry and pillar geometries, we apply the same counting procedure to obtain +1/2 and -1/2 defect positional frequencies across all frames. In the stairway geometry, we apply the counting procedure sequentially to each step and, for the pillar, the videos are processed by centring the pillar in a $400 \times 400\mu m^2$ window. Similar to the analysis done with the submersed trench, we use MATLAB to generate a 2D histogram to represent the frequency of the +1/2 and -1/2 defects, positionally distributed in a 2D plane. Defects are organised and binned every 13.4μm in both horizontal and vertical increments.

To measure the director orientation directly above trenches, the imaged active nematic is oriented with the long axis parallel to the y-axis. Each pixel is converted to micrometers (0.9434μm/pixel). Each pixel from each frame containing a x-component, y-component and angle of the bundle-microtubule director is represented on a 2D grid and determined using MATLAB. Our process uses a nested loop and a conditional statement to determine if the angle is between 80 and 90°; if a director satisfied this condition along the y-axis for the specified x-position, the total is summed then divided by the total number of angles checked by the loop. This probability is appended to a new horizontal array for each probability in the x-position. The result is a time-averaged director orientation mapped across the trench, averaging over all y values. The analysis is presented in **Figure 2**.

I.5. Simulations

To complement the experiments, we simulate the active nematic thin film using a 2D hybrid lattice Boltzmann/finite difference approach. The incompressible active nematic film flows with velocity $\boldsymbol{u}(\boldsymbol{r};t)$, has long-range orientational order described by the tensor order parameter $\boldsymbol{Q}(\boldsymbol{r};t)$ and varying concentrations of active material, which we take to be a phase field $\phi(\boldsymbol{r};t)$ varying from 0 to 1, coarsely describing the local amount of active materials (microtubules, kinesin complexes and ATP). Four coupled equations describe the time evolution of these continuous fields.

The first is the Beris-Edwards equation for nematics,

$$(\partial_t + \boldsymbol{u}\cdot\boldsymbol{\nabla})\boldsymbol{Q} - \boldsymbol{S} = \Gamma_Q \boldsymbol{H}. \tag{1}$$

The co-rotation term $\boldsymbol{S} = (\xi\boldsymbol{D}+\boldsymbol{\Omega})\left(\boldsymbol{Q}+\frac{1}{3}\boldsymbol{I}\right) + \left(\boldsymbol{Q}+\frac{1}{3}\boldsymbol{I}\right)(\xi\boldsymbol{D}-\boldsymbol{\Omega}) - 2\xi\left(\boldsymbol{Q}+\frac{1}{3}\boldsymbol{I}\right)\mathrm{tr}(\boldsymbol{QW})$ determines the alignment of the microtubules in response to gradients in the velocity field, with $\boldsymbol{\Omega}$ the rotational part and $\boldsymbol{D}$ is the extensional part of the velocity gradient tensor $\boldsymbol{W} = \boldsymbol{\nabla v} = \boldsymbol{\Omega} + \boldsymbol{D}$. The alignment parameter ξ is taken to be in the flow aligning regime and set to $\xi = 0.5$. The molecular field $\boldsymbol{H} = -(\frac{\delta\mathcal{F}}{\delta\boldsymbol{Q}} - \frac{1}{3}\boldsymbol{I}\ \mathrm{Tr}\frac{\delta\mathcal{F}}{\delta\boldsymbol{Q}})$ is a functional derivative of free energy $\mathcal{F}$, describing the relaxation towards equilibrium at a rate Γ_Q. The free energy depends directly on the nematic order $\boldsymbol{Q}$ and the active material concentration ϕ. The nematic part consists of a Landau-De Gennes contribution, $\mathcal{F}_{\mathrm{bulk,Q}} = A_0\left(\frac{1}{2}\left(1-\frac{\nu}{3}\right)\mathrm{tr}(\boldsymbol{Q}^2) - \frac{\nu}{3}\mathrm{tr}(\boldsymbol{Q}^3) + \frac{\nu}{4}\mathrm{tr}(\boldsymbol{Q}^2)^2\right)$, and deformation $\mathcal{F}_{\mathrm{grad,Q}} = \frac{K}{2}(\boldsymbol{\nabla Q})^2$. We set $\nu = 2.55$, which favours the isotropic state in the absence of active flows[53] and is independent of $\phi(\boldsymbol{r};t)$. This choice allows nematic ordering only due to activity-induced flows, in agreement with experiments[52] and previous simulations[53, 54].

The active material concentration evolves according to a Cahn-Hillard model. We assume that the film is incompressible and active material concentration ϕ does not impact fluid mass density ρ.

$$\partial_t\phi + \boldsymbol{\nabla}\cdot(\boldsymbol{u}\phi) = \Gamma_\phi\mu, \tag{2}$$

where $\mu = \frac{\delta\mathcal{F}}{\delta\phi} - \boldsymbol{\nabla}\cdot\left(\frac{\delta\mathcal{F}}{\delta\boldsymbol{\nabla}\phi}\right)$ is the chemical potential and Γ_ϕ is a mobility coefficient. The free energy depends on phase as $\mathcal{F}_{\mathrm{bulk},\phi} = \frac{A_\phi}{2}\phi^2(\phi-1)^2$ and a gradient term $\mathcal{F}_{\mathrm{grad},\phi} = \frac{K_\phi}{2}(\boldsymbol{\nabla}\phi)^2$. The free energy minima are at $\phi = \{0,1\}$. However, activity suppresses ordering and ϕ does not phase separate into high and low ϕ regions for sufficiently active flows. We initialise the concentration to $\phi = 0.5$. All reported phenomena are due to dynamical interactions, since the free energy does not favour global nematic ordering nor phase separation.

Lastly, the system obeys the Navier-Stokes equations for the velocity field within the active film. Assuming constant fluid mass density ρ (not active material concentration ϕ) leads to the incomprehensibility condition

$$\boldsymbol{\nabla}\cdot\boldsymbol{u} = 0. \tag{3}$$

Because the experimental active nematic film lies on a 2D interface between two 3D fluids, the planar divergence of the velocity could conceivably be non-zero. However, non-zero divergent velocity fields would require continuous circulation in the thin aqueous/oil layers above/below the film. As we are unaware of evidence indicating such flows, we assume 2D incomprehensibility implying divergence-free flow. Since the fluid is taken to be incompressible, any outward fluid mass flux into an enclosed area must be balanced by an inward flux and vice versa.

The second equation is the Cauchy momentum equation

$$\rho(\partial_t + \boldsymbol{u}\cdot\boldsymbol{\nabla})\boldsymbol{u} = -\boldsymbol{\nabla}p + \boldsymbol{\nabla}\cdot\boldsymbol{\Pi} - \gamma\boldsymbol{u}, \tag{4}$$

where p is the pressure and $\boldsymbol{\Pi}$ is the stress tensor which consists of the standard viscous stress $\boldsymbol{\Pi}^{\mathrm{visc}} = 2\eta\boldsymbol{E}$ for film viscosity η. Furthermore, it contains the elastic stress due to the nematic nature of the microtubules

$$\begin{aligned}\boldsymbol{\Pi}^{\mathrm{elastic}} = &-P\boldsymbol{I} + 2\lambda\boldsymbol{\mathcal{Q}}(\boldsymbol{Q}:\boldsymbol{H}) - \lambda\boldsymbol{H}\cdot\boldsymbol{\mathcal{Q}} - \lambda\boldsymbol{\mathcal{Q}}\cdot\boldsymbol{H}\\ &- \boldsymbol{\nabla Q}:\frac{\delta\mathcal{F}}{\delta\boldsymbol{\nabla Q}} + \boldsymbol{Q}\cdot\boldsymbol{H} - \boldsymbol{H}\cdot\boldsymbol{Q},\end{aligned} \tag{5}$$

and capilary stresses $\boldsymbol{\Pi}^{\mathrm{cap}} = (\mathcal{F}-\mu\phi)\boldsymbol{I} - \boldsymbol{\nabla}\phi\left(\frac{\delta\mathcal{F}}{\delta\boldsymbol{\nabla}\phi}\right)$ due to differences in concentration ϕ. The stress also contains

the active component

$$\mathbf{\Pi}^{\mathrm{act}} = -\zeta\left(\boldsymbol{r};t\right)\boldsymbol{Q} = -\zeta_0\phi\left(\boldsymbol{r};t\right)\boldsymbol{Q}. \tag{6}$$

Here, we have taken the local activity

$$\zeta\left(\boldsymbol{r};t\right) = \zeta_0\phi\left(\boldsymbol{r};t\right) \tag{7}$$

to scale directly with active material concentration.

In the Navier-Stokes equation, we also include an effective friction term $\gamma\left(\boldsymbol{r}\right)\boldsymbol{u}\left(\boldsymbol{r};t\right)$. Since previous studies have successfully modelled dynamics of microtubule/kinesin-based active nematic films with weak effective friction[55], we treat the friction as negligible in the regions of the film superjacent to deep structures. In the regions above shallows, we include lubrication momentum dissipation via a non-zero effective friction coefficient. We set $\gamma(h_s) = 0.07$ in the shallows for simulations of the trench system. We define a characteristic confinement scale to be $R \equiv 20$ LB nodes. The narrowest trench width is $w_t = 1.2R$ (**Figure 3**c) and the two wider trenches have widths of f $w_t = 1.7R$ (**Figure 3**b) and $6R$ (**Figure 3**d), respectively. All trenches are simulated in $7.5R \times 30R$ periodic systems. For the stairway, we simulate a $7.5R \times 50R$ long system composed of the same number of steps as in the experimental system (10 steps) of width $w_s = 5R$. Each step represents a different lubrication momentum dissipation region with different non-zero effective friction coefficients set to $\gamma(h_s, n) = \frac{0.1}{1+n}$, where $n \in \{0 \ldots 9\}$ denotes the different steps corresponding to different oil depths in the experiments. In the main text, we present data from steps $n = \{1, 2, 3, 4, 5\}$. For the pillars, we use a radius $r_p = R$. We observe depletion of ϕ for $\gamma(h_s) = 0.07$, corresponding to the choice used for the trench geometry, but present results for the larger value $\gamma(h_p) = 0.5$, as it better matches the pronounced depletion observed experimentally in **Figure 5**. The pillar is simulated in a $10R \times 10R$ periodic system.

II. REFERENCES

[1] D. DellArciprete, M. Blow, A. Brown, F. Farrell, J. S. Lintuvuori, A. McVey, D. Marenduzzo, and W. C. Poon, Nature Communications **9**, 1 (2018).
[2] Z. You, D. J. G. Pearce, A. Sengupta, and L. Giomi, Phys. Rev. X **8**, 031065 (2018).
[3] H. Li, X.-q. Shi, M. Huang, X. Chen, M. Xiao, C. Liu, H. Chaté, and H. P. Zhang, PNAS **116**, 777 (2019).
[4] D. van Holthe tot Echten, G. Nordemann, M. Wehrens, S. Tans, and T. Idema, arXiv , arXiv (2020).
[5] G. Duclos, C. Erlenkämper, J. Joanny, and P. Silberzan, Nature Physics **13**, 58 (2017).
[6] T. B. Saw, A. Doostmohammadi, V. Nier, L. Kocgozlu, S. Thampi, Y. Toyama, P. Marcq, C. T. Lim, J. M. Yeomans, and B. Ladoux, Nature **544**, 212 (2017).
[7] K. Kawaguchi, R. Kageyama, and M. Sano, Nature **545**, 327 (2017).
[8] G. Duclos, C. Blanch-Mercader, V. Yashunsky, G. Salbreux, J.-F. Joanny, J. Prost, and P. Silberzan, Nature Physics **14**, 728 (2018).
[9] C. Pérez-González, R. Alert, C. Blanch-Mercader, M. Gómez-González, T. Kolodziej, E. Bazellieres, J. Casademunt, and X. Trepat, Nature Physics **15**, 79 (2019).
[10] R. Zhang, N. Kumar, J. L. Ross, M. L. Gardel, and J. J. de Pablo, PNAS **112**, 15048 (2017).
[11] L. Huber, R. Suzuki, T. Krüger, E. Frey, and A. R. Bausch, Science **361**, 255 (2018).
[12] N. Kumar, R. Zhang, J. J. de Pablo, and M. L. Gardel, Science Advances **4** (2018).
[13] M. M. Norton, A. Baskaran, A. Opathalage, B. Langeslay, S. Fraden, A. Baskaran, and M. F. Hagan, Phys. Rev. E **97**, 012702 (2018).
[14] J. Hardoüin, J. Laurent, T. Lopez-Leon, J. Ignés-Mullol, and F. Sagués, Soft Matter **16**, 9230 (2020).
[15] H. Reinken, D. Nishiguchi, S. Heidenreich, A. Sokolov, M. Bär, S. H. Klapp, and I. S. Aranson, Communications Physics **3**, 1 (2020).
[16] B. Zhang, B. Hilton, C. Short, A. Souslov, and A. Snezhko, Phys. Rev. Research **2**, 043225 (2020).
[17] A. J. Tan, E. Roberts, S. A. Smith, U. A. Olvera, J. Arteaga, S. Fortini, K. A. Mitchell, and L. S. Hirst, Nature Physics **15**, 1033 (2019).
[18] E. Bertin, A. Baskaran, H. Chaté, and M. C. Marchetti, Phys. Rev. E **92**, 042141 (2015).
[19] A. M. Nagel, M. Greenberg, T. N. Shendruk, and H. W. de Haan, Scientific Reports **10**, 1 (2020).
[20] M. Bär, R. Großmann, S. Heidenreich, and F. Peruani, Annual Review of Condensed Matter Physics **11**, 441 (2020).
[21] M. N. van der Linden, L. C. Alexander, D. G. A. L. Aarts, and O. Dauchot, Phys. Rev. Lett. **123**, 098001 (2019).
[22] L. Caprini, U. Marini Bettolo Marconi, and A. Puglisi, Phys. Rev. Lett. **124**, 078001 (2020).
[23] R. Großmann, I. S. Aranson, and F. Peruani, Nature Communications **11**, 1 (2020).
[24] G. Mahmud, C. J. Campbell, K. J. M. Bishop, Y. A. Komarova, O. Chaga, S. Soh, S. Huda, K. Kandere-Grzybowska, and B. A. Grzybowski, Nat. Phys. **5**, 606 (2009).
[25] J. Katuri, D. Caballero, R. Voituriez, J. Samitier, and S. Sanchez, ACS Nano **12**, 7282 (2018).
[26] L. Angelani, R. Di Leonardo, and G. Ruocco, Phys. Rev. Lett. **102**, 048104 (2009).
[27] A. Sokolov, M. M. Apodaca, B. A. Grzybowski, and I. S. Aranson, PNAS **107**, 969 (2010).
[28] P. Pietzonka, E. Fodor, C. Lohrmann, M. E. Cates, and U. Seifert, Phys. Rev. X **9**, 041032 (2019).
[29] R. Sunyer and X. Trepat, Current Biology **30**, R383 (2020).
[30] E. A. Novikova, M. Raab, D. E. Discher, and C. Storm, Phys. Rev. Lett. **118**, 078103 (2017).
[31] K. Schakenraad, L. Ravazzano, N. Sarkar, J. A. J. Won-

dergem, R. M. H. Merks, and L. Giomi, Phys. Rev. E **101**, 032602 (2020).
[32] A. Sokolov, A. Mozaffari, R. Zhang, J. J. de Pablo, and A. Snezhko, Phys. Rev. X **9**, 031014 (2019).
[33] M. M. Norton, P. Grover, M. F. Hagan, and S. Fraden, Phys. Rev. Lett. **125**, 178005 (2020).
[34] D. P. Rivas, T. N. Shendruk, R. R. Henry, D. H. Reich, and R. L. Leheny, Soft Matter **16**, 9331 (2020).
[35] P. W. Ellis, D. J. Pearce, Y.-W. Chang, G. Goldsztein, L. Giomi, and A. Fernandez-Nieves, Nature Physics **14**, 85 (2018).
[36] D. J. G. Pearce, P. W. Ellis, A. Fernandez-Nieves, and L. Giomi, Phys. Rev. Lett. **122**, 168002 (2019).
[37] R. Zhang, S. A. Redford, P. V. Ruijgrok, N. Kumar, A. Mozaffari, S. Zemsky, A. R. Dinner, V. Vitelli, Z. Bryant, M. L. Gardel, and J. J. de Pablo, arXiv preprint arXiv:1912.01630 (2019).
[38] P. Guillamat, J. Ignés-Mullol, and F. Sagués, Nature Communications **8**, 1 (2017).
[39] T. N. Shendruk, A. Doostmohammadi, K. Thijssen, and J. M. Yeomans, Soft Matter **13**, 3853 (2017).
[40] A. Doostmohammadi, T. N. Shendruk, K. Thijssen, and J. M. Yeomans, Nature Communications **8** (2017).
[41] S. Chandragiri, A. Doostmohammadi, J. M. Yeomans, and S. P. Thampi, Soft Matter **15**, 1597 (2019).
[42] J. Hardoüin, R. Hughes, A. Doostmohammadi, J. Laurent, T. Lopez-Leon, J. M. Yeomans, J. Ignés-Mullol, and F. Sagués, Communications Physics **2**, 1 (2019).
[43] L. M. Pismen and F. Sagués, The European Physical Journal E **40**, 92 (2017).
[44] R. Alert, J.-F. Joanny, and J. Casademunt, Nature Physics **16**, 682 (2020).
[45] K. Thijssen, M. R. Nejad, and J. M. Yeomans, Phys. Rev. Lett. **125**, 218004 (2020).
[46] A. Opathalage, M. M. Norton, M. P. N. Juniper, B. Langeslay, S. A. Aghvami, S. Fraden, and Z. Dogic, PNAS **116**, 4788 (2019).
[47] F. Kempf, R. Mueller, E. Frey, J. M. Yeomans, and A. Doostmohammadi, Soft Matter **15**, 7538 (2019).
[48] R. Aditi Simha and S. Ramaswamy, Phys. Rev. Lett. **89**, 058101 (2002).
[49] L. Giomi, L. Mahadevan, B. Chakraborty, and M. F. Hagan, Phys. Rev. Lett. **106**, 218101 (2011).
[50] B. Martínez-Prat, J. Ignés-Mullol, J. Casademunt, and F. Sagués, Nature Physics **15**, 362 (2019).
[51] P. Guillamat, J. Ignés-Mullol, S. Shankar, M. C. Marchetti, and F. Sagués, Phys. Rev. E **94**, 060602 (2016).
[52] T. Sanchez, D. T. N. Chen, S. J. DeCamp, M. Heymann, and Z. Dogic, Nature **491**, 431 (2012).
[53] S. P. Thampi, A. Doostmohammadi, R. Golestanian, and J. M. Yeomans, EPL (Europhysics Letters) **112**, 28004 (2015).
[54] P. Srivastava, P. Mishra, and M. C. Marchetti, Soft Matter **12**, 8214 (2016).
[55] Z. Zhou, C. Joshi, R. Liu, M. M. Norton, L. Lemma, Z. Dogic, M. F. Hagan, S. Fraden, and P. Hong, Soft Matter , (2020).

ACKNOWLEDGEMENTS

We thank Amin Doostmohammadi for helpful discussions. We acknowledge generous funding from the National Science Foundation, through several awards (DMR-1808926), NSF-CREST: Center for Cellular and Biomolecular Machines at UC Merced (HRD-1547848), and from the Brandeis Biomaterials facility MRSEC-1420382. K.T. acknowledges funding from the European Unions Horizon 2020 research and innovation programme under the Marie Sklodowska-Curie grant agreement no. 722497 (LubISS). T.N.S received funding from the European Unions Horizon 2020 research and innovation programme (grant agreement no. 851196).

AUTHOR CONTRIBUTIONS

L.S.H conceptualised the project. L.S.H and T.N.S designed the study [TNS: add a boston person here?]. L.S.H, D.K., S.F and M.A.G. all contributed to the design of experiments, and T.N.S., J.M.Y and K.T. contributed to the design of the simulations. S.A.A. made all the surfaces [TNS: "all"?]. D.K. performed experiments [TNS: experiments from Boston performed by?] and K.T. implemented simulations. D.K. and K.T. performed data analysis. T.N.S. and L.H.S. wrote the paper with assistance from J.M.Y., D.K. and K.T., and input from S.F and M.A.G. All authors discussed and interpreted results and revised the paper.

COMPETING INTERESTS

The authors declare no competing interests.

III. SUPPLEMENTARY INFORMATION

III.1. Sinusoidal Microstructures

To demonstrate that the method of submersing micropatterned substrates in the oil layer below an active nematic film can guide defect dynamics, we produced a series of micropattern sinusoidal substrates (**Methods I.3**). The smallest of these are characterised by amplitude $\Delta_u = 40 \pm 2\mu$m and wavelength $\lambda_u = 150 \pm 2\mu$m. As observed in **Movie M3** and discussed in the main text, the undulating effective friction produces orientation-control of motile defects for smaller wavelengths. Trains of co-aligned $+1/2$ defects move along the troughs (**Figure S1**a). However, these are intermittently disrupted by the extensile-active nematic hydrodynamic-bend instability. Regions of well-ordered nematic aligned along the troughs results in pair creation events in which $+1/2$ defects unbind with an orientation perpendicular to the troughs (**Figure S1**b).

III.2. Rectangular Microstructure Pillar

Simulations of rectangular pillar (**Figure S2**) exhibit a comparable depletion of concentration ϕ from the en-

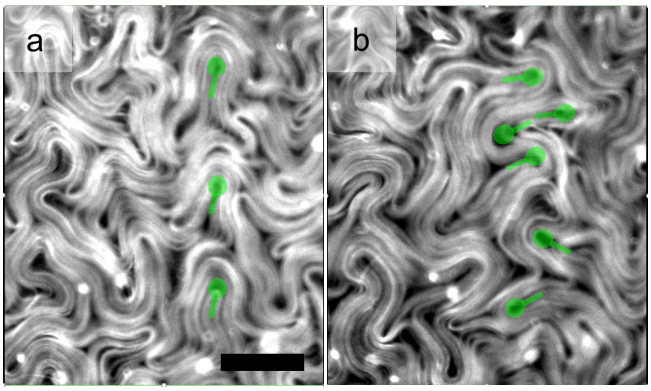

FIG. S1: **Submersed micropatterned sinusoidal substrate.** Fluorescent image of the active nematic film superjacent to an oil-submersed sinusoidal micropatterned structure with a 300µm pitch and a 30µm amplitude. The undulated go from left to right such that the parallel troughs and crests run in parallel up and down. Scale bar = 250µm. (a) A set of three motile +1/2 defects marked in green that move in a train up the middle of a trough. The train aligns the director parallel to the trench. (b) 15sec later the initial train is destabilised by extensile-active nematic hydrodynamic-bend instability and associated pair creation events in which +1/2 defects tend to unbind oriented perpendicular to the trough.

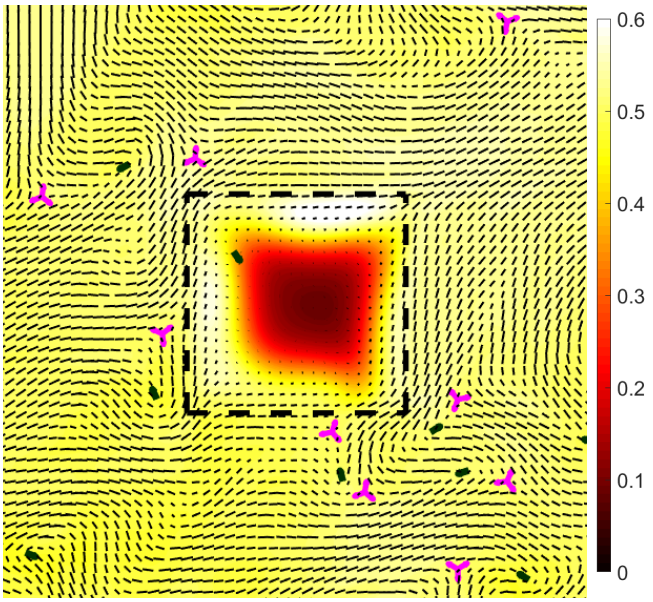

FIG. S2: **Rectangular pillar causes depletion.** Same as **Figure 1**i but with the circular pillar replaced with a square, the perimeter of which is traced by dashed lines. We observe a comparable degree of depletion of active material concentration ϕ, denoted by the colormap, for the same friction coefficient $\gamma = 0.5$.

closed area above the pillar as the circular pillars considered in the main text (**Figure 5**). Hence, we conclude that a pillar curvature is not the critical property leading to depletion in the pillar geometry. Rather, the abrupt gradient in S that follows indirectly from the increased effective friction produces a radially outward average active force that can deplete active material from any enclosed area of high effective friction.

III.3. Microstructure Pit

In the main text, we argue that active material is depleted from the enclosed region directly above a microstructured pillar due to the increased effective viscous dissipation within the locally thinner oil-layer. Thus, one naturally wonders if a microstructured pit in the substrate might act as an "anti-pillar" and lead to accumulation of active material within an enclosed region above the structure. We consider an effective circular pit by simulating a substrate with an effective friction except directly above the structure (**Figure S3**) and observe that active material accumulates in the enclosed area. The velocity magnitude, nematic scalar order parameter, and concentration directly above the pit (**Figure 3**) are all comparable to their values far from the pillar (**Figure 5**,a,b,d respectively). While the change in the scalar order parameter is positively peaked at the perimeter of the pillar (**Figure 5**c), it is seen to dip at the perimeter of the pit (**Figure 3**). This indicates a radially inward average active force, consistent with the mechanism which here leads to accumulation.

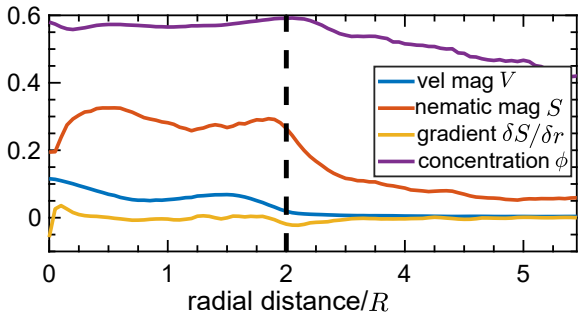

FIG. S3: **Pits cause local lower friction regions which result in active matter accumulation.** We consider a circular pit of radius $2R$ above which the frictional damping is negligible but outside of which $\gamma = 0.1$). We measure the same profiles as **Figure 5**a-d for one instant after steady state has been achieved. We observe accumulation of active material ϕ in the enclosed area.

III.4. Movie Captions

M1 Micropatterned trench geometry. Fluorescence microscopy video of a bundled microtubule/kinesin network at 1mM ATP at the oil-water interface above a submersed SU-8 substrate with a micropatterned trench. The trench possesses a depth 8 ± 1µm and width $w_t = 327 \pm 2$µm. Left and right are shallow regions which exhibit active turbulence, while the centre is the deep region, the edges of which form a well-defined virtual boundary that traps defects.

M2 Simulation results of a repeating lattice of counter-rotating vortices above a trench. The trench width is $w_t = 1.7R$. Plus-half defects (dark green) are trapped between the virtual boundaries, generating the repeating vortex structure along the centre line that is distinct from the active turbulence that exists outside the virtual boundaries. In the colormap, blue (red) denotes clock (anti-clock) wise rotating vortices.

M3 Micropatterned sinusoid geometry. Fluorescence microscopy video of a bundled microtubule/kinesin active nematic network above an oil-submersed sinusoidal microstructure with a 300µm pitch and a 30µm amplitude. The undulated go from left to right such that the parallel troughs and crests run in parallel up and down. Train of +1/2 defects move up and down the troughs but are unstable to intermediate pair creation and unbinding events oriented perpendicular to the troughs.

M4 Micropatterned sinusoid geometry. The same as **Movie M3** but for a microstructure with a 500µm pitch and a 50µm amplitude. Distinct trains of +1/2 are not as immediately apparent but nonetheless self-propelled defects tend to align with the troughs. [TNS: Does movie need a scale bar?]

M5 Micropatterned stairway geometry. Fluorescence microscopy video of a bundled microtubule/kinesin film over an oil-submersed, micropatterned stairway. Individual steps are 500µm wide and 10µm tall. The oil depth from left to right progresses from $h - h_0 = \{50, 60, 70, 80, 90\}$µm sequentially where the initial fluid depth is $h_0 = 12 \pm 3$µm.

M6 Micropatterned pillar geometry. Fluorescence microscopy video of a bundled microtubule/kinesin network at the oil-water interface with 1mM ATP above a substrate possessing a micropatterned pillar of radius $r_p = 116 \pm 2$µm and height $h_p = 6.8 \pm 0.3$µm. The bundled microtubule/kinesin network in the film directly above the immersed pillar is fully depleted. Annihilation events can be observed as +1/2 approach the boundary and annihilate with perimeter-associated -1/2 defects.

M7 Simulation results of the active nematic film above a pillar illustrating depletion of active material. Active matter concentration ϕ (denoted by colormap) is initialised uniformly but over time is depleted from the region inside the circle with high friction ($f = 0.5$). The director field is illustrated with black lines and the plus-half defects and minus-half defects are denoted by dark green and magenta circles, respectively.

M8 Simulation results of defect dynamics around a pillar that acts as a virtual obstacle. Plus-half defects (dark green) deflect from the depleted high-friction region or are absorbed by minus-half defects (magenta) when approaching the pillar structure. On the other hand, pair production in the vicinity of the pillar typically creates radially outward-oriented self-motile +1/2 defects that leave immotile -1/2 defects near the virtual perimeter.

M9 Micropatterned pillar with +1/2 defect entering depletion zone. The same as **Movie M6** but exhibiting an instance of active material in the superjacent film crossing the boundary above the pillar.